CHINESE OPTICS LETTERS

Vol. 20, No. 10 | October 2022

Experimental investigation on the unbalanced Mach–Zehnder interferometer on lithium niobate thin film

Xuerui Sun (孙雪芮)[1,†], Yinan Wu (吴忆南)[1,†], Chuanyi Lu (卢川艺)[1], Yuting Zhang (张玉婷)[1], Hao Li (黎 浩)[1], Shijie Liu (刘时杰)[1], Yuanlin Zheng (郑远林)[1,2*], and Xianfeng Chen (陈险峰)[1,2,3**]

[1] State Key Laboratory of Advanced Optical Communication Systems and Networks, School of Physics and Astronomy, Shanghai Jiao Tong University, Shanghai 200240, China

[2] Shanghai Research Center for Quantum Sciences, Shanghai 201315, China

[3] Collaborative Innovation Center of Light Manipulation and Applications, Shandong Normal University, Jinan 250358, China

*Corresponding author: ylzheng@sjtu.edu.cn

**Corresponding author: xfchen@sjtu.edu.cn

Received March 5, 2022 | Accepted May 25, 2022 | Posted Online June 25, 2022

We design and fabricate an unbalanced Mach–Zehnder interferometer (MZI) via electron beam lithography and inductively coupled plasma etching on lithium niobate thin film. The single unbalanced MZI exhibits a maximum extinction ratio of 32.4 dB and a low extra loss of 1.14 dB at the telecommunication band. Furthermore, tunability of the unbalanced MZI by harnessing the thermo-optic and electro-optic effect is investigated, achieving a linear tuning efficiency of 42.8 pm/°C and 55.2 pm/V, respectively. The demonstrated structure has applications for sensing and filtering in photonic integrated circuits.

Keywords: lithium niobate; Mach–Zehnder interferometer; electro-optic effect; thermo-optic effect; nanowaveguide.
DOI: 10.3788/COL202220.101301

1. Introduction

Integrated photonics on lithium niobate thin film (LNTF) has emerged as an outstanding approach for on-chip scalable optical signal manipulation and processing, which has attracted widespread attention and stimulated tremendous enthusiasm in recent years[1–5]. Lithium niobate (LN) exhibits excellent properties, such as wide transparent window, low intrinsic absorption, extraordinary second-order nonlinearity, and large electro-optics[6]. Other than exceptional optical properties of LN, LNTF provides the capability for dense integration of photonic integrated circuits (PICs) on the novel platform while being compatible with conventional CMOS technology, resulting in various compact and superior devices that are inaccessible to their conventional counterparts. With the advancement in micro- and nanofabrication technology, a variety of high-performance devices on LNTF, based on nanowaveguides, microresonators, and photonic crystal structures, have been reported for applications in modulators[7–11], filters[12,13], polarization controllers[14], frequency convertors[15–18], quantum sources[19–21], and so forth.

As one critical component among integration applications, the Mach–Zehnder interferometer (MZI), which can be balanced or unbalanced, has a wide range of applications. Amplitude modulators based on the balanced MZI structure are ubiquitous and play a significant role in optical switching, processing, and communication[1–4,7,8,14]. Unbalanced MZIs (UMZIs), on the other hand, can be used to implement wavelength sensitive devices, such as comb filters or interleavers[22], which have been demonstrated as the key component of sensors, filters, spectrometers in photonics, and neural and network applications[23,24]. UMZIs on LNTF are particularly suitable for such tunable devices, as thermo-optic and electro-optic effects can be easily incorporated into the devices.

Here, we report on an optimized UMZI designed and fabricated in LNTF via electron beam lithography (EBL) and inductively coupled plasma (ICP) etching. A high extinction ratio (ER) of 32.4 dB and a low extra loss (EL) of 1.14 dB are obtained on the basis of the total interferometer. Both the thermo-optic and electro-optic tunability of the fabricated UMZI is experimentally investigated. A linear tuning efficiency of 42.8 pm/°C and 55.2 pm/V is obtained. The demonstrated structure has applications for sensing and filtering in PICs on the novel platform.

2. Device Design, Fabrication, and Characterization

In our design, the UMZI on x-cut LNTF is composed of two 1×2 symmetric multimode interference (MMI) couplers and

two bent waveguide segments of unequal length, as illustrated in Fig. 1(a). The propagation of light in the UMZI is mainly along the y axis. The input light is firstly launched into the first MMI coupler, which serves as a 3 dB coupler. Then, the two beams with equal light intensity from the first MMI coupler, after traveling through two unbalanced arms, are coherently combined in the second MMI coupler. Figure 1(b) shows the 3D schematic of the designed MMI coupler, as well as notation for the dimension. The working principle of the MMI coupler is based on the self-imaging effect[25]. MMI couplers are favored over Y shaped beam couplers due to their small size, broad bandwidth, well-proportioned splitting ratio, and large fabrication tolerance. The equal splitting ratio of MMI couplers and ultralow propagation loss of the waveguide are critical in achieving the high ER of the MZI. The phase difference $\Delta\Phi$ between the two arms at the output is $\Delta\Phi = 2\pi n_{\text{eff}}(\lambda)\Delta L/\lambda$, where n_{eff} is the effective refractive index, λ is the wavelength in vacuum, ΔL is the length difference of the two arms, and $\Delta L = 406.8\ \mu\text{m}$ in our experiment. The free spectral range (FSR) can be calculated by using $\text{FSR}(\lambda) \approx \lambda^2/[\Delta L \cdot n_g(\lambda)]$, in which n_g is the group index. The corresponding FSR at 1550 nm is 2.47 nm. The output intensity of the MZI is given by $I_{\text{out}} = I_{\text{in}}[1 + \cos(\beta\Delta L)]$, where I_{in} and I_{out} are defined as the intensities of the input and output, respectively. β is the propagation constant of light in the waveguide, which varies with the temperature and applied electric field due to refractive index change via thermo-optic and electro-optic effects, respectively.

Figure 1(c) shows the calculated effective index n_{eff} of the different optical modes, TE_0, TM_0, TE_1, TM_1, TE_2, and TM_2 modes, as a function of the waveguide width, w_{wg}. The height of the waveguide, i.e., the LNTF thickness $(h_1 + h_2)$, is 600 nm, which is the same as the experimental condition. The etching height of the ridge nanowaveguide is half of the LNTF thickness. Single mode propagation is guaranteed when the waveguide width is narrower than 1 μm. To guarantee single mode propagation, the width of the nanowaveguide is set to be 700 nm, taking into consideration both the MMI structure and the fabrication conditions. Inferring from Fig. 1(c), we choose the width of the MMI coupler, w_{MMI}, to be 2.8 μm, because it allows for the simultaneous existence of TE_0 and TE_1 modes while avoiding other higher-order ones, which corresponds to the boundary of the blue area in the diagram. Then, the EL of the MMI coupler, i.e., the on-chip insertion loss, is calculated with respect to its length. The MMI coupler shows the lowest EL at the length of 5.0–5.5 μm. As indicated by the simulation in Fig. 1(d), the excess loss is kept less than 0.3 dB when the MMI's length varies from 4.5 to 6.5 μm, showing a large fabrication tolerance. The inset shows the simulated light propagation along a 5.3-μm-long MMI coupler.

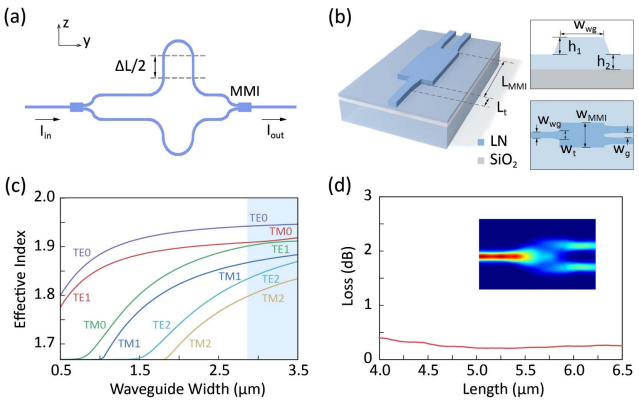

Fig. 1. (a) Schematic of the UMZI with a length difference of ΔL. MMI, multimode interference coupler. (b) Schematic of the MMI from different view angles. (c) Calculated effective index n_{eff} of optical modes versus the ridge waveguide width with an air upper cladding. (d) Calculated loss of the MMI with respect to its length. The MMI width is 2.80 μm.

In our experiment, the UMZIs, together with referencing MMI couplers and straight waveguides, are fabricated by EBL and ICP etching techniques on the same LNTF sample. The fabrication procedure starts from a commercial x-cut LNTF wafer (NANOLN, Jinan Jingzheng Electronics Co., Ltd.) with 600-nm-thick LN, 2-μm-thick silica, and 500-μm-thick LN substrate. In order to achieve the etching depth of LN, amorphous silicon is selected as the mask, which has an appropriate selectivity ratio for LN etching. Firstly, 580-nm-thick amorphous silicon is deposited on the LNTF through plasma enhanced chemical vapor deposition (PECVD). Then, a layer of resist is spin-coated on the surface of the sample, and the structures are patterned using EBL. The mask layer patterns are subsequently transferred to the LNTF via ICP etching twice. The residual mask is finally removed by wet etching to form the designed structures. The main part of the fabrication process was done at the Center for Advanced Electronic Materials and Devices (AEMD), Shanghai Jiao Tong University.

The integration of compact MMI beam couplers and low-loss waveguides is important in high-performance MZIs. Firstly, the loss of individual MMI couplers is experimentally investigated, where a straight waveguide is used as a reference. The MMI coupler shows low loss in a wide span, as shown in Fig. 2. The wavelength span is limited by the used tunable laser in our experiment. The experimental EL is less than 1.5 dB over the whole span, with a loss of roughly 0.4 dB at 1550 nm. The

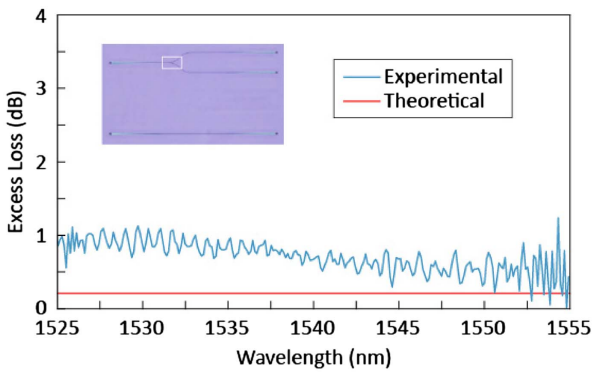

Fig. 2. Experimentally measured EL of the MMI coupler. Inset: optical microscopy image of the MMI coupler.

calculated loss is about 0.2 dB over a broad band starting from 1500 to 1600 nm.

3. Results and Discussion

Other than the well-proportioned splitting ratio of the MMI couplers, both arms of the MZI are bent to balance the extra bending loss in order to achieve a high ER. Figure 3 shows an optical microscopy image of the fabricated UMZI. A straight waveguide is used as reference to measure the EL of the UMZI. Light is coupled into the waveguide through grating coupling. It should be noted that the grating coupler itself has a high degree of polarization dependence. The input/output grating coupler is optimized for the TE mode only, so TM modes experience a large loss in the device. The grating couplers have a period of 0.85 μm and a duty cycle of 0.33 for maximum efficiency at the wavelength of 1550 nm. The SEM image of the grating coupler is shown in the upper left inset of Fig. 3(a). The upper right inset shows the SEM image of the compact 50:50 MMI components with a length of 5.31 μm and a width of 2.80 μm. To reduce the coupling loss between the fiber and the waveguide, an adiabatically tapered waveguide is manufactured to connect the interferometer and the grating coupler. Figure 3(b) is the SEM image of the cross-sectional view of the nanowaveguide. The top width of the fabricated ridge waveguide is 700 nm with an etching depth of about 325 nm, with an etched sidewall inclination angle of about 65 deg. Figure 3(c) indicates the simulated electric field distribution of the TE_0 mode at 1550 nm when the top width of the nanowaveguide is 700 nm.

An amplified spontaneous emission (ASE) light source centered at 1550 nm with a 50 nm bandwidth is used to measure the spectral response of the UMZI at room temperature. The normalized transmission spectrum of the TE-polarized light is shown in Fig. 4(a). The achieved ER in the whole span of ASE ranges from 20 to over 30 dB. A high ER of 32.4 dB is achieved at the wavelength of 1539.5 nm. The high ER of the individual UMZI without cascading configuration indicates that the split ratio of the MMI couplers is close to the ideal parameter, and bending loss is well balanced. This is comparable with the highest demonstrated ER on LNTF to date[7,8,26]. Figure 4(b) presents the enlarged transmission spectrum of the UMZI, showing an FSR of 2.53 nm, which is close to the theoretical prediction of 2.47 nm. The EL of the interferometer is measured to be 1.14 dB.

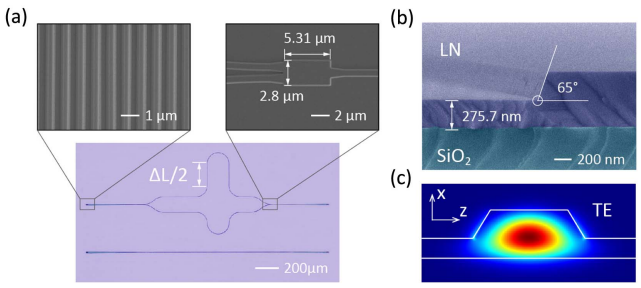

Fig. 3. (a) Optical microscope image of the UMZI. Insets: SEM images of the grating coupler and MMI components, respectively. (b) False-color SEM image of the cross section of the ridge waveguide. (c) The simulation of the fundamental TE mode at 1550 nm.

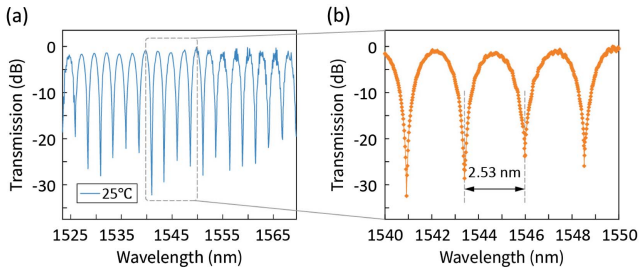

Fig. 4. Normalized transmission spectrum of the fabricated UMZI.

To characterize the thermal tunability, we measured normalized transmission spectra of the UMZI at different temperatures. The result is displayed in Fig. 5(a). As can be seen, a temperature variation from 20°C to 70°C causes a total redshift of the spectrum by 2.14 nm. The FSR at different temperatures is marked as demonstrated in Figs. 5(b) and 5(c), inferring negligible variance. Figure 5(c) also shows that the normalized transmission spectra exhibit a highly linear shift with a slope of 42.8 pm/°C. More efficient control approach of thermo-optic tuning may rely on metal micro-heaters[27,28]. Sensitivity to fabrication errors comes with the strong confinement of the LNTF nanowaveguides. Tunability based on the strong thermo-optic response can ease the stringent precision requirement of the devices during the design and fabrication, allowing for larger tolerance. The FSR of the UMZI exhibits negligible change with respect to the varying temperature, which indicates that the UMZI has the necessary stability in terms of linear operation with thermo-optic modulation. The relation of output power and temperature at the wavelength of 1534.34 nm is displayed in Fig. 5(d). The theoretical curve of output I_{out} is consistent with the experimental data. It can be derived that the variation of the refractive

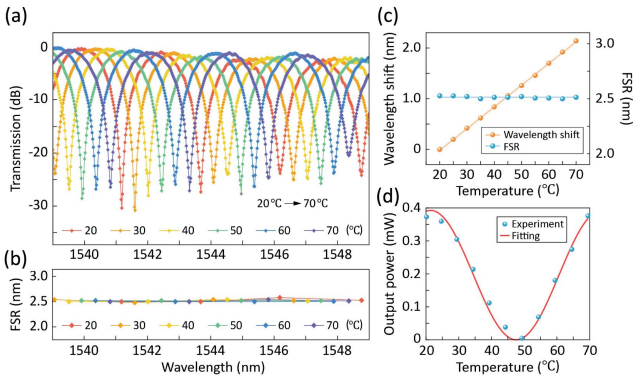

Fig. 5. (a) Thermo-optic tuning performance of the UMZI. (b) The FSRs of the UMZI at temperatures from 20°C to 70°C. (c) Wavelength shift and FSR as a function of the temperature. (d) The measured output power varying with temperature and its fitting curve at 1534.34 nm.

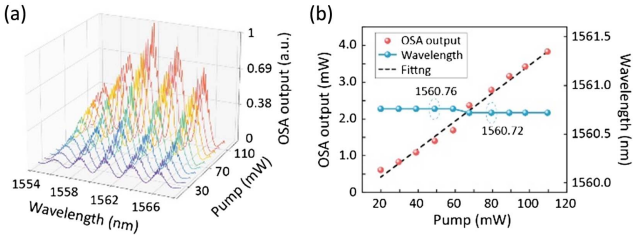

Fig. 6. (a) Measured transmitted optical spectrum analyzer (OSA) spectra as a function of input power. (b) Maximum output signal and its wavelength versus input power.

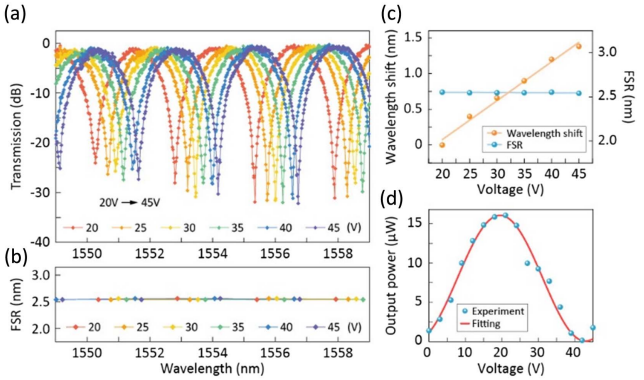

Fig. 7. (a) Electro-optical tuning performance of the UMZI. (b) The FSRs of the UMZI at voltages from 20 V to 45 V. (c) Wavelength shift and FSR as a function of the voltage. (d) The measured output power varying with voltage and its fitting curve at 1549.3 nm.

index versus temperature is approximately 3.0×10^{-5} °C^{-1}, which is between the thermo-optic coefficients of LN (3.34×10^{-5} °C^{-1}) and silica (0.95×10^{-5} °C^{-1}).

The output versus the varying input power at room temperature is investigated to demonstrate the stability of the UMZI under high optical powers, as displayed in Fig. 6(a). The wavelength corresponding to the peak transmitted power is approximately 1560.7 nm. The dependence of the maximum output power and the corresponding wavelength on the input is shown in Fig. 6(b). The wavelength is nearly unchanged with the increase of the input power, except for a tiny shift at 60 mW. Notably, the UMZI performs stably at large input optical powers, due to ultralow propagation loss of the nanowaveguides.

As presented above, the UMZI on LNTF can achieve a comparatively large ER and a relatively low EL. Modulation based on the UMZI can also utilize the electro-optic effect of LN, which is important in optical modulators, electric field sensing[24], on-chip spectrometers, etc.

Furthermore, active tuning is also implemented through the electro-optic effect. For electro-optic tuning, the UMZI is similar to the previous one. The arm path of the unbalanced MZI is extended by 2 mm, and the path difference is kept the same. A gold electrode with a thickness of 200 nm and a spacing of 6 μm (with a 20-nm-thick Cr adhesive layer) is deposited to one arm of the UMZI. The length of the electrode is 2 mm. The image of the sample is not shown in the figure. The electric field is applied along the z axis to access the largest electro-optic coefficient of γ_{33}. The transmission shifts due to the electrically induced phase difference between the two arms via the electro-optic effect. The electrically tuned transmission of the UMZI is demonstrated in Fig. 7. Normalized transmission spectra are recorded at different DC bias voltages ranging from 20 V to 45 V, which covers the half-wave voltage V_π of the device. A total wavelength shift of 1.38 nm is generated by the loaded DC bias voltage, and the V_π is estimated to be 20 V accordingly. Figures 7(b) and 7(c) characterize the FSR at different voltages, which stays constant. The shift of the normalized transmission spectrum is linearly related to the bias voltage with a tuning slope of 55.2 pm/V, as shown in Fig. 7(c). We confirm the V_π of the UMZI by changing the voltage while detecting the output power at a fixed wavelength of 1549.3 nm, which is provided with an initial phase difference at zero bias of π, and the measured V_π is 21 V, as shown in Fig. 7(d). If the optical signal is modulated on both arms simultaneously with the push–pull configuration, the half-wave voltage can be reduced by a factor of two, corresponding to a quality factor $V_\pi L$ of 2.1 V·cm. This can be further improved by using a thicker electrode and a narrower electrode gap. Besides, the electro-optic effect has a much faster response than thermo-optic effect and is adopted in ultra-high-speed optical modulation in MZIs[7–9,29]. For UMZIs the electro-optic modulation also has the advantage of fast response, which is critical in optical switching, electric field sensing, and microwave filtering applications. Besides, it can be expected that the combination of thermo-optic and electro-optic effects in a tandem manner may lead to greater device tunability for wider application scenarios.

4. Conclusion

In summary, we report on the design and fabrication of UMZIs on LNTF via EBL and ICP etching processes. The UMZIs experimentally achieve a high ER of 32.4 dB and an EL of 1.14 dB in the telecommunication band. A linear shift with a tuning slope of 42.8 pm/°C and 55.2 pm/V is obtained by harnessing the strong thermo-optic and electro-optic effects of LN. The working wavelength of the UMZI is almost independent of the incident power, which verifies the ultralow propagation loss of the waveguides. The UMZI can be used as a basic structure for a variety of optical components in PICs to achieve wide applications.

Acknowledgement

This work was supported by the National Natural Science Foundation of China (Nos. 12074252, 62022058, 62005159, and 11734011), National Key Research and Development Program of China (Nos. 2017YFA0303701 and 2018YFA0306301), Shanghai Municipal Science and Technology Major Project (No. 2019SHZDZX01-ZX06), Shanghai Rising-Star Program (No. 20QA1405400), and Shanghai Jiao Tong University

(No. 21X010200828). We thank the Center for Advanced Electronic Materials and Devices (AEMD) of Shanghai Jiao Tong University for the assistance of device fabrication.

†These authors contributed equally to this work.

References

1. A. Boes, B. Corcoran, L. Chang, J. Bowers, and A. Mitchell, "Status and potential of lithium niobate on insulator (LNOI) for photonic integrated circuits," Laser Photonics Rev. **12**, 1700256 (2018).
2. J. Lin, F. Bo, Y. Cheng, and J. Xu, "Advances in on-chip photonic devices based on lithium niobate on insulator," Photonics Res. **8**, 1910 (2020).
3. D. Zhu, L. Shao, M. Yu, R. Cheng, B. Desiatov, C. J. Xin, Y. Hu, J. Holzgrafe, S. Ghosh, A. Shams-Ansari, E. Puma, N. Sinclair, C. Reimer, M. Zhang, and M. Lončar, "Integrated photonics on thin-film lithium niobate," Adv. Opt. Photonics **13**, 242 (2021).
4. Y. Qi and Y. Li, "Integrated lithium niobate photonics," Nanophotonics **9**, 1287 (2020).
5. Y. Zheng and X. Chen, "Nonlinear wave mixing in lithium niobate thin film," Adv. Phys. **6**, 1889402 (2021).
6. D. N. Nikogosyan, *Nonlinear Optical Crystals: A Complete Survey* (Springer Science & Business Media, 2006).
7. C. Wang, M. Zhang, X. Chen, M. Bertrand, A. Shams-Ansari, S. Chandrasekhar, P. Winzer, and M. Lončar, "Integrated lithium niobate electro-optic modulators operating at CMOS-compatible voltages," Nature **562**, 101 (2018).
8. M. Xu, M. He, H. Zhang, J. Jian, Y. Pan, X. Liu, L. Chen, X. Meng, H. Chen, Z. Li, X. Xiao, S. Yu, S. Yu, and X. Cai, "High-performance coherent optical modulators based on thin-film lithium niobate platform," Nat. Commun. **11**, 3911 (2020).
9. M. Li, J. Ling, Y. He, U. A. Javid, S. Xue, and Q. Lin, "Lithium niobate photonic-crystal electro-optic modulator," Nat. Commun. **11**, 4123 (2020).
10. M. Xu, M. He, Y. Zhu, L. Liu, L. Chen, S. Yu, and X. Cai, "Integrated thin film lithium niobate Fabry–Perot modulator [Invited]," Chin. Opt. Lett. **19**, 060003 (2021).
11. X. Liu, B. Xiong, C. Sun, J. Wang, Z. Hao, L. Wang, Y. Han, H. Li, J. Yu, and Y. Luo, "Wideband thin-film lithium niobate modulator with low half-wave-voltage length product," Chin. Opt. Lett. **19**, 060016 (2021).
12. K. Abdelsalam, E. Ordouie, M. G. Vazimali, F. A. Juneghani, P. Kumar, G. S. Kanter, and S. Fathpour, "Tunable dual-channel ultra-narrowband Bragg grating filter on thin-film lithium niobate," Opt. Lett. **46**, 2730 (2021).
13. A. Prencipe, M. A. Baghban, and K. Gallo, "Tunable ultranarrowband grating filters in thin-film lithium niobate," ACS Photonics **8**, 2923 (2021).
14. Z. Lin, Y. Lin, H. Li, M. Xu, M. He, W. Ke, H. Tan, Y. Han, Z. Li, D. Wang, X. S. Yao, S. Fu, S. Yu, and X. Cai, "High performance polarization management devices based on thin-film lithium niobate," Light Sci. Appl. **11**, 93 (2022).
15. C. Wang, C. Langrock, A. Marandi, M. Jankowski, M. Zhang, B. Desiatov, M. M. Fejer, and M. Lončar, "Ultrahigh-efficiency wavelength conversion in nanophotonic periodically poled lithium niobate waveguides," Optica **5**, 1438 (2018).
16. R. Luo, Y. He, H. Liang, M. Li, and Q. Lin, "Highly tunable efficient second-harmonic generation in a lithium niobate nanophotonic waveguide," Optica **5**, 1006 (2018).
17. M. Yu, B. Desiatov, Y. Okawachi, A. L. Gaeta, and M. Lončar, "Coherent two-octave-spanning supercontinuum generation in lithium-niobate waveguides," Opt. Lett. **44**, 1222 (2019).
18. J. Lu, J. B. Surya, X. Liu, Y. Xu, and H. X. Tang, "Octave-spanning supercontinuum generation in nanoscale lithium niobate waveguides," Opt. Lett. **44**, 1492 (2019).
19. Z. Ma, J.-Y. Chen, Z. Li, C. Tang, Y. M. Sua, H. Fan, and Y.-P. Huang, "Ultrabright quantum photon sources on chip," Phys. Rev. Lett. **125**, 263602 (2020).
20. J. Zhao, C. Ma, M. Rüsing, and S. Mookherjea, "High quality entangled photon pair generation in periodically poled thin-film lithium niobate waveguides," Phys. Rev. Lett. **124**, 163603 (2020).
21. U. A. Javid, J. Ling, J. Staffa, M. Li, Y. He, and Q. Lin, "Ultrabroadband entangled photons on a nanophotonic chip," Phys. Rev. Lett. **127**, 183601 (2021).
22. X. P. Li, K. X. Chen, and L. F. Wang, "Compact and electro-optic tunable interleaver in lithium niobate thin film," Opt. Lett. **43**, 3610 (2018).
23. H. Jung, "An integrated photonic electric-field sensor utilizing a 1× 2 YBB Mach–Zehnder interferometric modulator with a titanium-diffused lithium niobate waveguide and a dipole patch antenna," Crystals **9**, 459 (2019).
24. C. Gutierrez-Martinez, J. Santos-Aguilar, J. Meza-Pérez, and A. Morales-Díaz, "Novel electric field sensing scheme using integrated optics $LiNbO_3$ unbalanced Mach–Zehnder interferometers and optical delay-modulation," J. Light. Technol. **35**, 27 (2017).
25. L. B. Soldano and E. C. Pennings, "Optical multi-mode interference devices based on self-imaging: principles and applications," J. Light. Technol. **13**, 615 (1995).
26. M. Jin, J.-Y. Chen, Y. M. Sua, and Y.-P. Huang, "High-extinction electro-optic modulation on lithium niobate thin film," Opt. Lett. **44**, 1265 (2019).
27. X. Liu, P. Ying, X. Zhong, J. Xu, Y. Han, S. Yu, and X. Cai, "Highly efficient thermo-optic tunable micro-ring resonator based on an LNOI platform," Opt. Lett. **45**, 6318 (2020).
28. G. Chen, H.-L. Lin, J. D. Ng, and A. J. Danner, "Integrated thermally tuned Mach–Zehnder interferometer in z-cut lithium niobate thin film," IEEE Photon. Technol. Lett. **33**, 664 (2021).
29. J. Hu, C. Li, C. Guo, C. Lu, A. P. T. Lau, P. Chen, and L. Liu, "Folded thin-film lithium niobate modulator based on a poled Mach–Zehnder interferometer structure," Opt. Lett. **46**, 2940 (2021).